

A Review of Experimental Techniques for Gravitational Wave Detection at LIGO

Yuan Shi

30 April, 2018

Abstract

The Laser Interferometer Gravitational Wave Observatory (LIGO) is designed to detect gravitational waves from distant astrophysical sources in the frequency range from 10 Hz to 10 kHz. After a series of sensitivity upgrades, Advanced LIGO achieved a strain sensitivity of better than $10^{-23}/\sqrt{\text{Hz}}$ at 100 Hz, and its first observation run between September 2015 and January 2016 has culminated in the first direct detection of gravitational waves from a black hole coalescence, GW150914, on 14th September 2015. This review introduces the experimental techniques and the underlying physics concepts used in Advanced LIGO that have made this detection possible. In particular, techniques targeting reduction of seismic, thermal and quantum noises are of central importance to the sensitivity upgrades that have been achieved. This includes upgrades in passive and active seismic isolation techniques, test mass suspension and coating designs, power recycling and the addition of signal recycling.

1 Introduction

The possibility of using interferometers as gravitational wave detectors was first considered in the early 1960s[3]. Over several decades, this vision developed into the first generation of LIGO detectors ('Initial LIGO') located in Hanford and Livingston, and its European partners, Virgo (French-Italian) and GEO 600 (Germany-UK) detectors[4, 5], all targeting gravitational waves in the audio frequency band, from 10 Hz to 10 kHz. Initial LIGO detectors were operational until 2010, but no gravitational wave was detected by Initial LIGO.

Compared to Initial LIGO, the second generation Advanced LIGO is designed to be 10 times more sensitive over a broad frequency band, and to extend the low end of the detection band to from 40 Hz to 10 Hz[6]. Among the various noise sources that limit LIGO sensitivity, this review focuses on seismic noise, thermal noise and quantum noise - the three dominant sources that have posed major challenges at Advanced LIGO - and reviews the experimental techniques implemented to minimise these noises. Section 2 gives a brief introduction on the workings of the gravitational wave interferometer, its sensitivity requirements and major noise contributions. Section 3 explains seismic noise and techniques to reduce it, including active control and feedback systems and passive suspension system. Section 4 reviews LIGO designs that reduce different types of thermal noise - suspension thermal noise, coating and substrate Brownian noise. Section 5 introduces quantum noise including shot noise and radiation pressure noise, and describes power and signal recycling as techniques used for quantum noise reduction.

2 The Gravitational Wave Interferometer

2.1 Overview of the Interferometer

Gravitational waves propagate as strains in space that lead to tiny deformations of mechanical systems. The strain produced on a mechanical system of length l undergoing a change in length δl is defined as $\delta l/l$, which is directly proportional to the gravitational wave amplitude h . The quadrupole nature of gravitational radiation leads to two orthogonal polarizations of the wave at 45° to each other, of amplitude h_+ and h_\times , and each of these produces a strain in space in the relevant directions, as illustrated in Fig. 1 (left).

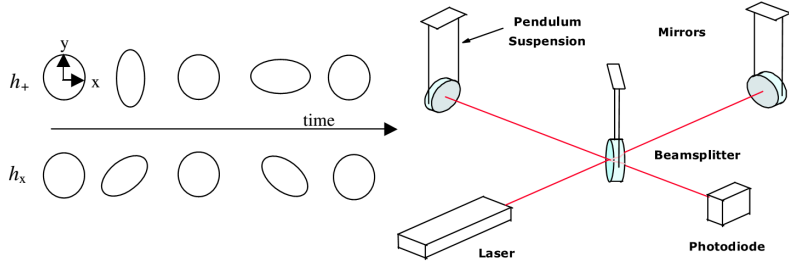


Figure 1: Left: time variation of strains in space for the two directions of polarisation of gravitational waves. Right: A simplified set up of a basic Michelson interferometer. (Figure adapted from [7])

In its essence, the gravitational wave interferometer is a Laser Michelson interferometer formed between freely hanging mirrors ('test masses') in vacuum 4 km apart, forming Fabry-Perot cavities to further scale up the optical path length within the cavities, as shown in Fig. 2. The interferometer undergoes a differential change in its arm lengths when interacting with gravitational waves if the mirrors lie on the same plane with rings of deformation, as shown in Fig. 1. The induced differential arm length results in small changes in the intensity of the light observed at the interferometer output, which are the signals of gravitational waves.

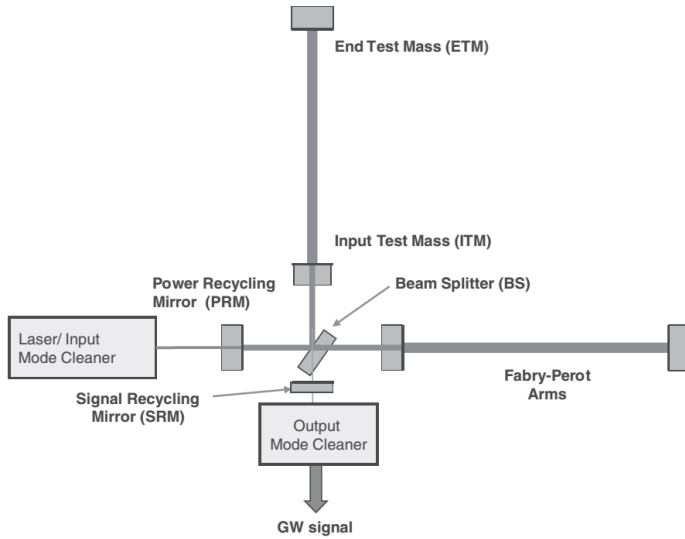


Figure 2: A simplified schematic diagram of the Advanced LIGO interferometer. The four test masses forms a Michelson interferometer with 4 km long Fabry-Perot arm cavities. The power and signal recycling mirrors are installed to minimise quantum noise and enhance signal (more on this in Section 5). The output mode cleaner acts as a signal filter to transmit the signal field on the carrier light as much as possible, while removing any other irrelevant field.

2.2 Sensitivity Requirements and Noise Sources

Sensitivity and noise performance of LIGO is usually measured in terms of displacement or strain spectral density, with units m/\sqrt{Hz} and $/\sqrt{Hz}$ respectively. The displacement spectral density can be converted into an equivalent strain spectral density by dividing by the interferometer arm length. A lower value in displacement or strain spectral density represents lower noise level, higher sensitivity and thus better performance.

The real difficulty of detecting gravitational waves is that the predicted strains due to gravitational waves in space at the earth are typically of the order of 10^{-21} or smaller[7]. In order to observe a full range of sources, therefore, a sensitivity or noise performance in strain of below $10^{-23}/\sqrt{Hz}$ has to be achieved over most of the proposed operating range from 10 Hz to a few kilohertz. For an interferometer with an arm length of 4km, the required differential arm motion due to unwanted noise is $\delta x \leq 10^{-19}m/\sqrt{Hz}$ at 10 Hz and $\delta x \leq 2 \times 10^{-20}m/\sqrt{Hz}$ at 100 Hz in order to make gravitational wave signal differentiable - a formidable noise performance requirement for Advanced LIGO.

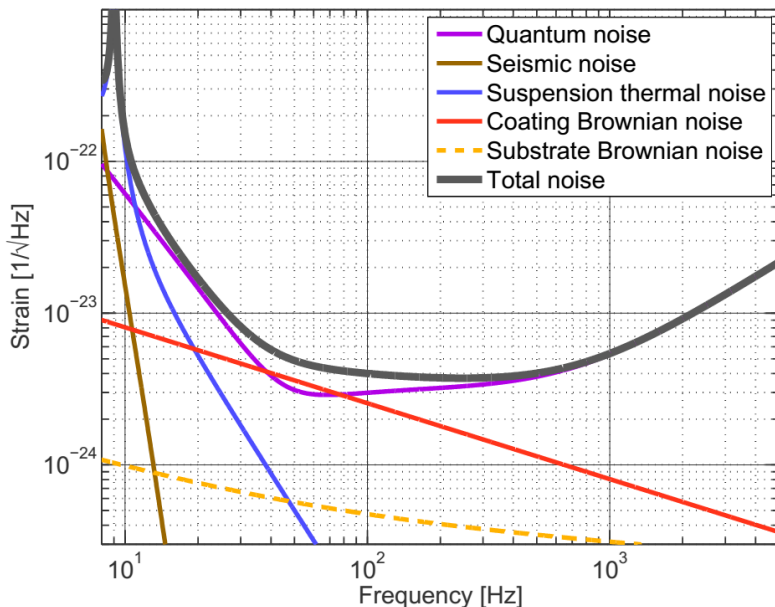


Figure 3: Noise contributions of the major noise sources at Advanced LIGO. Lower values correspond to higher sensitivities and better performances. (Adapted from [8])

As shown in Fig. 3, there are mainly three dominant noise sources LIGO has to tackle: seismic noise, thermal noise (including suspension thermal noise, coating Brownian noise, substrate Brownian noise), and quantum noise. Below 10 Hz, the sensitivity is limited by seismic noise and suspension thermal noise. Quantum noise dominates at most of the intermediate and high frequencies, and at frequencies between 40-100 Hz thermal noises (mainly coasting Brownian noise) dominates. The following sections delve into details on how the above noises arise and the relevant noise reduction techniques that have proved successful.

3 Seismic Noise

3.1 Noise Sources

Seismic noise is a type of noise introduced by ambient ground motions and vibrations due to natural causes (e.g. earthquakes, ocean waves) and human activities. These seismic disturbances interact with LIGO instruments through contact and lead to vibrational noises in the test masses. As the detection of gravitational wave signals requires precise measurements of the exact positions of the test masses, seismic noise is a problematic noise source for ground-based gravitational wave detectors.

The displacement spectral density of ground motions is roughly proportional to f^{-2} , where f is the frequency of motion:

$$\Delta \tilde{X}(f) \sim 10^{-7} \times \left(\frac{1}{f^2} \right) m/\sqrt{\text{Hz}} \quad (3.1)$$

in both horizontal and vertical directions[9, 10], which makes seismic noise a prominent noise source at low frequencies, as demonstrated in Fig.3. At LIGO, seismic noise has been significantly reduced by filtering through an upgraded seismic isolation system down to frequencies as low as $f \sim 3 \text{ Hz}$ [11] and is negligible above 11 Hz[6]. Techniques used to isolate seismic noise will be explored in the next section.

Besides seismic noise, seismic motion also introduces another type of noise called the gravitational gradient noise, or 'Newtonian noise'. Unlike seismic noise, which is induced through contact, gravitational gradient noise is caused by fluctuations in the ambient gravitational field as a result of seismic motion, which exerts a varying force noise on the test mass. While it is possible to isolate the system from seismic noise, no feasible technique has been developed so far to 'isolate' the system from gravitational gradient noise - a changing gravitational field (see Appendix A).

3.2 Reducing Seismic Noise

3.2.1 Overview

The seismic isolation system is a major upgrade made in Advanced LIGO. It involves both passive and active isolation: passive isolation makes use of mechanical linkages that absorb and damp the noise; active isolation involves sensors and actuators that counteract the noise through feedback and feed-forward control.

There are three linked systems providing multiple stages of seismic isolation to the test masses, as shown on the right of Fig. 4.

The first system is the Hydraulic External Pre-Isolator (HEPI). It is an active platform providing the first stage of active isolation. The second system is the Internal Seismic Isolation (ISI) platform that combines both active and passive isolation. The test masses are suspended from the down-facing ISI platform through a suspension system. It consists of three linked pendulums providing passive isolation to the test mass, which is suspended at the last stage. Together, they form the third and last 'quadruple' suspension system. [12, 13]

The isolation effect of each stage of isolation is illustrated in Fig. 4. As shown in Fig. 4, the entire isolation system reduces seismic noise to below $10^{-20} m/\sqrt{\text{Hz}}$ at 10 Hz, which extends the lower bound of the detection band from 40 Hz to 10 Hz.

HEPI and ISI use similar active isolation schemes through control and feedback systems, which will be explained in Section 3.2.2. Section 3.2.3 explains the working of the quadruple pendulum suspension for passive isolation.

3.2.2 Control and feedback systems of passive-active isolation platforms

The passive-active concept used in Advanced LIGO isolation platforms can be summarized by the schematic diagram in Fig. 5. The active feedback and control system involves the feed-forward and feedback inertial sensor, relative motion sensor and the control force generated by the actuators (3,4,5,6 in Fig. 5). These instruments form a feedback block and a feed-forward block to actively counteract seismic noise. This scheme is outlined below and illustrated Fig. 6.

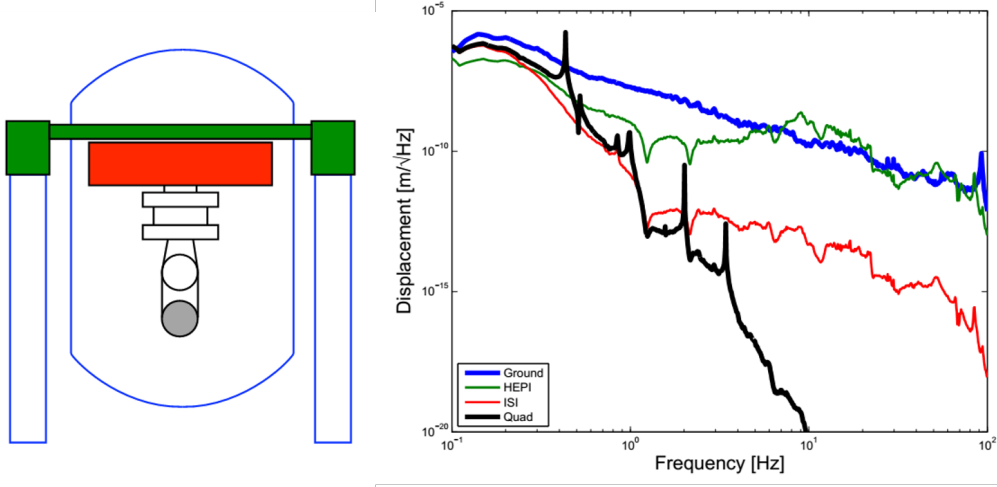


Figure 4: Left: schematic diagram of the configuration of three isolation stages: HEPI, ISI and quadruple suspension (labeled ‘Quad’). Right: seismic isolation contribution from the three isolation stages; colours on the right match those of the curves on the left. At very low frequencies, HEPI reduces the motion between 0.1 and 5 Hz by a factor of 10. The ISI system reduces ground motion by a factor of ~ 300 at 1 Hz and ~ 3000 at 10 Hz[8]. Together with quadruple pendulum suspensions, which provide an isolation factor of $\sim 1/f^8$ (see Section 3.2.3), the Advanced LIGO isolation systems reduce the seismic-induced test mass motion by 10 to 11 orders of magnitude, from $10^{-9}m/\sqrt{Hz}$ (cf. Eqn.3.1) to below $10^{-20}m/\sqrt{Hz}$ at 10 Hz, bringing the seismic cut-off frequency (the frequency beyond which the noise is significantly reduced) from 40 Hz to 10 Hz. [1, 12] (Figure adapted from [8])

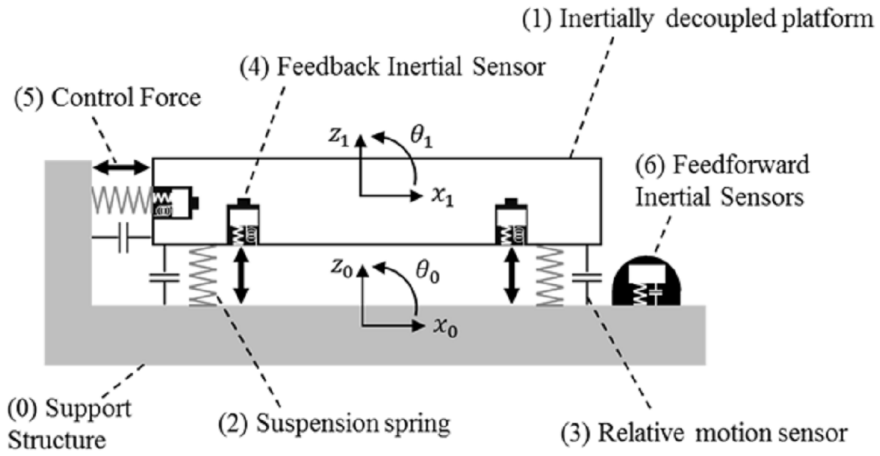


Figure 5: A schematic diagram of the active-passive isolation platform. The motion disturbance transmitted by the support structure (including previous isolation stages) is shown in grey (0). The isolation platform (1) is supported by suspension springs (2) with low natural frequencies to decouple the platform from the input stage through passive isolation beyond resonance frequency. Relative sensors (3), feedback inertial sensors (4) and feed-forward inertial sensors (6) measure displacements of the isolation platform and their signals combine to drive the control forces of the actuators(5). Components (3)-(6) together constitute the active control and feedback system. (Figure adapted from [12])

According to Fig. 6, the displacement spectral density of input seismic noise is denoted as $X_0(f)$, and that of the reduced output seismic noise of the isolation platform is $X_1(f)$ (blue arrows). The feed-forward and feedback controllers send force signals $F_{FB}(f)$ and $F_{FF}(f)$ to the actuator, which counteracts X_0 . The counteracting displacement induced by the actuator exerting a force $F(f)$ is $X_A(f) = P_A(f)F(f)$, where P_A is the force transfer function, or the ‘actuator path’[12].

The resultant platform motion X_1 is thus given by

$$X_1 = X_0 + P_A F. \quad (3.2)$$

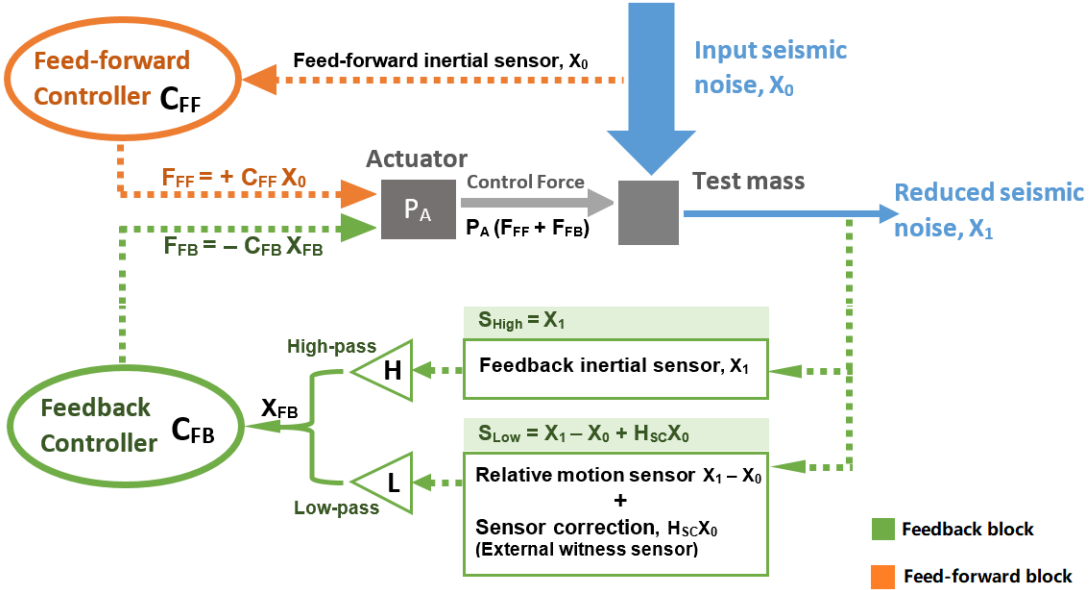


Figure 6: Feedback(green) and feed-forward(orange) schemes in active isolation. The actuator combines the feedback and feed-forward signals and apply a control force to counteract test mass motion due to external seismic noise, X_0 . The ideal outcome should be a close-to-zero seismic noise after isolation, X_1 .

In the feedback block (green), for output platform motions at higher frequencies ($f > 0.3$ Hz), X_1 is measured by the feedback inertial sensors as S_{High} and passed through a high-pass filter with transfer function $H(f)$. The high-pass filter is needed because the inertial sensors are AC-coupled and therefore do not give accurate readings at very low frequencies.

At low frequencies, relative sensors are used instead to measure the differential motion between the output and the input motion, $X_1 - X_0$. Value of X_1 is then obtained via sensor correction[14], where an external ground instrument, the witness sensor, directly measures X_0 . Ideally, adding measurements from relative sensors and sensor correction would give $S_{Low} = X_1$. However, the witness sensor is also noise-limited at low frequencies, and is therefore filtered through another high-pass filter, $H_{SC}(f)$, giving

$$S_{Low} = X_1 - X_0 + H_{SC}X_0 \quad (3.3)$$

S_{Low} is then passed through a complementary low-pass filter, $L(f)$, which satisfies

$$L(f) + H(f) = 1 \quad (3.4)$$

at all frequencies.

The combined signal, X_{FB} , is fed into the feedback controller with open loop gain C_{FB} , which then determines the control force F_{FB} :

$$F_{FB} = -C_{FB}X_{FB} \quad (3.5)$$

where $X_{FB} = H \cdot S_{High} + L \cdot S_{Low}$ ($S_{High} = X_1$)

Without feed-forward control, the resultant control force, $F = F_{FB}$. Substituting Eqn. 3.3-3.5 into Eqn. 3.2 and dividing both sides by X_0 gives the seismic noise transmissibility as

$$\begin{aligned}\frac{X_1}{X_0} &= \frac{1 + LC_{FB}P_A(1 - H_{SC})}{1 + C_{FB}P_A} \\ &\approx L(1 - H_{SC}) \quad \text{if } C_{FB} \rightarrow \infty\end{aligned}\tag{3.6}$$

To minimise X_1/X_0 at a broad range of frequencies, $H_{SC}(f)$, the low pass filter $L(f)$ (and its complementary high pass filter) are therefore tuned to obtain a suitable compromise between effective isolation and sensor noise injection.

In addition, the non-zero residual seismic noise in Eqn. 3.6 can be canceled using the feed-forward controller[59] $C_{FF}(f)$ as shown in Fig. 6. With the feed-forward controller, the control force becomes

$$F = F_{FB} + F_{FF}, \quad \text{where } F_{FF} = +C_{FF}X_0\tag{3.7}$$

Addition of the feed-forward controller introduces an additional term to Eqn. 3.6:

$$\frac{X_1}{X_0}(\text{with FF}) = \frac{1 + LC_{FB}P_A(1 - H_{SC}) + P_A C_{FF}}{1 + C_{FB}P_A}\tag{3.8}$$

An ideal feed-forward filter, therefore, is designed so that

$$C_{FF} = -\frac{1}{P_A} - L C_{FB}(1 - H_{SC}),\tag{3.9}$$

which, when substituted into Eqn. 3.8, gives $X_1/X_0 = 0$.

Seismic noise can thus be completely nulled in theory, although in practice this stage of isolation is limited by sensor noise, especially at frequencies below 3 Hz[12].

3.2.3 Passive isolation of the quadruple pendulum system

The last stage of isolation comes from placing the mirror on the final stage of a quadruple pendulum system, in contrast to the single pendulum suspension of initial LIGO[16] and triple pendulums of GEO 600[17], as shown in Fig 7.

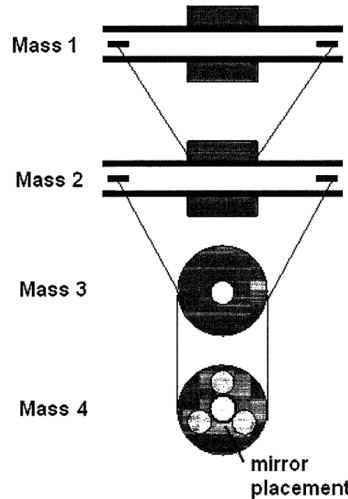


Figure 7: A simplified schematic diagram of the quadruple pendulum system, the last stage ('mirror placement') being the test mass. (Figure modified from [19])

Recall that the resonance response of a forced damped harmonic oscillator is given by

$$A(\omega) = \frac{F/m}{\sqrt{(\omega_0^2 - \omega^2)^2 + (\omega/\tau)^2}}$$

where τ is the damping time, ω_0 is the natural frequency of the pendulum and F is the applied force. Above the apparatus' resonant frequency f_0 , the resonance response falls off as f^{-2} , where f is the driving frequency. The pendulum's response to a driving displacement at the point of suspension thus has a similar dependence on frequency, characterised by the displacement transfer function (isolation factor), $T(f)$, which is shown[10, 18] to obey

$$T(f) = \frac{x_{\text{pendulum}}}{x_{\text{drive}}} \sim \left(\frac{f_0}{f} \right)^2$$

when $f > f_0$ for a single pendulum.

To increase isolation Advanced LIGO uses four pendulums in series including the test mass. The resonant frequencies of the suspension are kept low within a band from 0.4 to 4 Hz[20]. As the motion of one mass of a pendulum depends on the motion of the masses immediately above and below, the transfer function of the quadruple pendulum suspension will fall off as

$$T(f) \sim \prod_{i=1}^4 \left(\frac{f_i}{f} \right)^2 \sim \frac{1}{f^8}$$

where f_i is the resonance frequency of each pendulum.

In addition, damping through active feedback[19, 20] is also introduced to avoid excessive displacements at resonance frequencies. Fig. 8 shows the transfer functions for the quadruple pendulum in the longitudinal direction (along the direction of the arm length) with and without active damping. The quadruple suspension has an isolation factor of $\sim 4 \times 10^{-7}$ in the longitudinal dimension and $\sim 4 \times 10^{-4}$ in the vertical dimension at 10 Hz. With the target noise level and vertical-longitudinal cross-coupling taken into account, the target sensitivity level of $10^{-19} m/\sqrt{Hz}$ is achieved for both dimensions.[20]

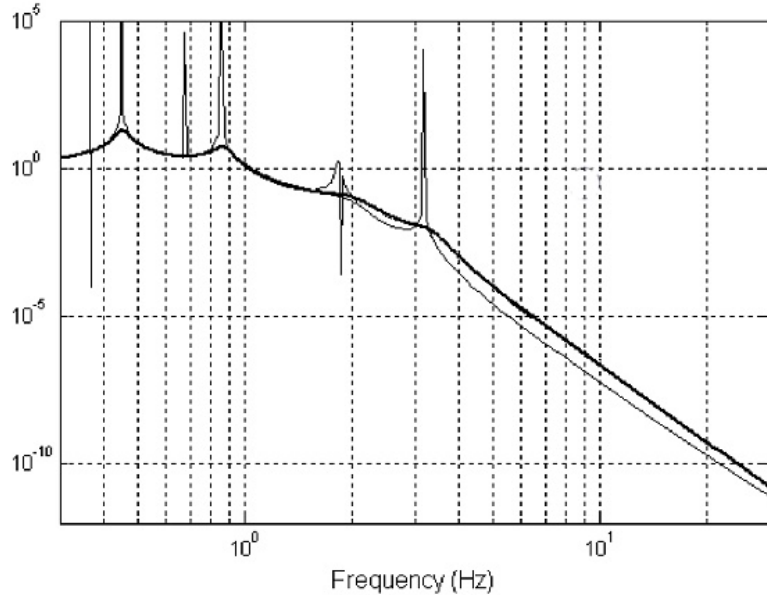


Figure 8: Longitudinal displacement transfer function of the suspension system, showing an isolation factor of $\sim 10^{-7}$ at 10 Hz. Bold line: with active damping; thin line: without active damping. (Figure adapted from [20])

While the pendulum suspension provides a satisfactory level of seismic isolation based on relatively simple principles, it introduces suspension thermal noise, and most of its complicated designs are tailored towards minimising this noise. This will be elaborated in the next section on thermal noise.

4 Thermal Noise

4.1 Noise Source

Thermal noise refers to random deviations of LIGO instruments from their thermal equilibrium states, caused by energy dissipation from random motion of the atoms (Brownian motion) of the core optics and the test masses.

Three sources of dissipation dominate the thermal noise at Advanced LIGO , coming from particle Brownian motions in the suspension fibres of the quadruple pendulums, the dielectric coatings of the test mass and, to a lesser extent, the substrate of the test mass. Thermal noises caused by these dissipative sources are called suspension thermal noise, dielectric coating Brownian noise and substrate Brownian noise respectively, as shown in Fig. 3.

Thermal noise is analytically modeled by the fluctuation-dissipation theorem (see below).

- **Fluctuation-dissipation theorem**

Whenever a particle is immersed in a dissipative environment, it is subject to statistical fluctuations around equilibrium, i.e. thermal noise. At equilibrium, the fluctuation-dissipation theorem quantifies the relation between thermal noise and energy dissipation (due to internal frictions and damping dragging particles in Brownian motion) as follows.

The power spectral density¹ of the randomly fluctuating thermal driving force $f(\omega)$ which describes random interactions between the particles within a material is shown to relate to internal energy dissipation in the same material by[21, 22]

$$f^2(\omega) = 4k_B T \Re\{Z(\omega)\}, \quad (4.1)$$

where k_B is the Boltzmann constant and T is the temperature. Z is the complex mechanical impedance of the material defined by $Z(\omega) = f(\omega)/v(\omega)$, where $v(\omega)$ is the velocity response to the thermal driving force. The real part of mechanical impedance is the resistivity of the material - a parameter that quantifies internal dissipation. Eqn. 4.1 shows that the thermal driving force is proportional to temperature (i.e. kinetic energy of the particles) and the level of internal dissipation.

Next, define the mechanical admittance of the material, $Y(\omega)$, to be

$$Y(\omega) = \frac{1}{Z(\omega)} \equiv \frac{v(\omega)}{f(\omega)} = \frac{i\omega x(\omega)}{f(\omega)}, \quad (4.2)$$

where $x(\omega)$ are steady state displacement response of the material to the thermal driving force $f(\omega)$.

Combining Eqn. 4.1 and 4.2, the power spectral density of thermal noise can be found given the real part of the mechanical admittance $Y(\omega)$, using

$$x^2(\omega) = \frac{4k_B T}{\omega^2} \Re\{Y(\omega)\}. \quad (4.3)$$

- **Suspension thermal noise**

For suspension thermal noise, the dissipative drag force $F(\omega)$ due to internal damping and dissipation in the suspension fibres with spring constant k and test mass of mass m is found to obey an extension of Hooke's law[23] , which can be approximated using

$$F(\omega) = -k[1 + i\phi(\omega)]x \quad \text{where } k = m\omega_0^2, \quad (4.4)$$

where ω_0 is the resonant frequency, and $\phi(\omega)$ is called the loss angle of the material (or the 'lag angle'), a parameter that quantifies the level of thermal dissipation. The equation of motion caused by internal dissipation in a material is thus

$$m\ddot{x}(t) - F(t) = f(t) \quad (4.5)$$

¹Spectral densities here still refer to the conventional 1-Hz bandwidth; using 1 rad/s bandwidth with angular frequencies, like Callen and Welton did in [22], would give an additional multiplier of $1/2\pi$

in the time domain where f is the random thermal driving force. In the frequency domain, using Eqn. 4.4, Eqn. 4.5 becomes

$$m[-\omega^2 + \omega_0^2\{1 + i\phi(\omega)\}]x(\omega) = f(\omega), \quad (4.6)$$

According to Eqn. 4.2 and 4.3, Eqn 4.6 gives

$$Y(\omega) = \frac{i\omega}{m((\omega_0^2 - \omega^2) + i\omega_0^2\phi(\omega))}, \quad (4.7)$$

and thus the displacement spectral density of suspension thermal noise $x(\omega)$:

$$x^2(\omega) = \frac{4k_B T \omega_0^2 \phi(\omega)}{\omega m[(\omega^2 - \omega_0^2)^2 + \omega_0^4 \phi^2]} \approx \frac{4k_B T \omega_0^2 \phi(\omega)}{m \omega^5} \quad \text{when } \omega \gg \omega_0 \quad (4.8)$$

• Coating and substrate Brownian noise

For both coating and substrate Brownian noise, the power spectral density of thermal noise (expressed in terms of frequency $f = 2\pi/\omega$ instead of ω) is also derived from Eqn. 4.3. It can be shown to be[24, 25, 26]

$$x^2(f) = \frac{2k_B T}{\pi^{3/2} f} \frac{1 - \sigma_s^2}{r Y_s} \phi_{\text{eff}}, \quad (4.9)$$

where r is the half-width of the Gaussian laser beam, σ_s and Y_s are Poisson ratio and Young's modulus of the material. The power spectral density is proportional to effective loss angle of the mirror, ϕ_{eff} . ϕ_{eff} includes contributions from both the substrate and the coatings[27], but it has been shown (for example, by Penn's experiment[28]) that the loss in the fused silica substrate ϕ_s is insignificant (2-3%) compared to the loss angle of the coating ϕ_c , so that $\phi_{\text{eff}} \approx \phi_c \gg \phi_s$.

Thermal noise is thus analytically calculated as above based on measurements of the losses of materials $\phi(\omega)$. Suspension thermal noise contributes to the detector noise below 30 Hz, limiting the low-frequency sensitivity to $h \approx 2 \times 10^{-21} f^{-1/2}/\sqrt{\text{Hz}}$. The test mass substrate has very low loss and correspondingly low fluctuations, contributing to the strain noise at $h \approx 3 \times 10^{-24} f^{-1/2}/\sqrt{\text{Hz}}$. Thermal noise from the dielectric mirror coatings exceeds that of the substrate by nearly an order of magnitude and limits the detector noise between 40 and 140 Hz, the most sensitive region to $h \approx 2.5 \times 10^{-23} f^{-1/2}/\sqrt{\text{Hz}}$. [8] Together, thermal noise contributes to final measurement noise of Advanced LIGO, but is below current sensitivity by a factor of ≥ 3 [1].

4.2 Reducing Thermal Noise

Reducing thermal noise requires minimisation of thermal loss², $\phi(\omega)$. As a result, the detector mirror and suspensions are fabricated from fused silica, an ultra-low mechanical loss material with near-zero coefficient of thermal expansion and high resistance to thermal fluctuations. It has been proved to have a sufficiently low loss compared to other metals to permit a significant reduction in thermal noise[31, 32].

The last two stages of the pendulum suspension form a monolithic (one-piece) fused silica stage, as illustrated in Fig. 9. The monolithic design allows the low mechanical loss of the test mass mirror to be preserved by avoiding contact with higher loss metal wires and potential friction at metal wire clamping and break-off points on the test mass[33], which used to introduce unwanted noise at Initial LIGO. The test masses are actuated (see Section 3.2.2) using a non-contact, low-force and low-noise electrostatic drive.[8]

Moreover, the suspension fibre and mirror coating designs are both optimised to minimise thermal noise, which is described in the next two sections.

²Another obvious option is to cool the test masses. While cryogenic cooling has been proposed[29], no cooling is currently used at LIGO. It has been used by some other gravitational wave detectors, however, such as the Japanese KAGRA detector[30].

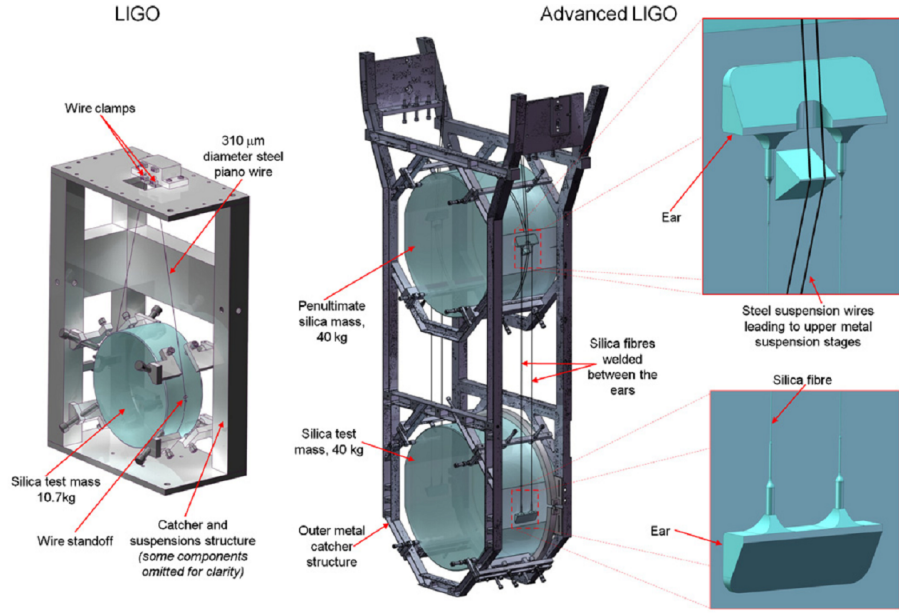


Figure 9: Initial LIGO single mirror suspension with steel wires v.s. Advanced LIGO’s monolithic fused silica suspension stage. The monolithic suspension consists of the penultimate silica mass, the last-stage silica test mass and silica suspension fibres. The fused silica attachment ears attach the fibres via welds, and the ears are attached to the mass sides via hydroxide-catalysis bonds[34], so that thermal loss at the joints are eliminated and contact with lossy steel wires is avoided. (Figure adapted from [34])

4.2.1 Reducing suspension thermal noise

The power spectral density of suspension thermal noise is given by Equation 4.6. To minimize $x^2(\omega)$ requires the lowest possible mechanical loss $\phi(\omega)$ in the fibre. As a result, the detector mirror suspensions are fabricated from fused silica, an ultra-low mechanical loss material with a very low coefficient of thermal expansion.

The dominant contributor to the mechanical loss of a fused silica fibre is thermoelastic loss, which occurs due to local spontaneous temperature fluctuations causing one side of the fibre to be heated or cooled and subsequently bending to occur in the fibre. The corresponding loss angle is shown[35] to obey the relation

$$\phi_{thermoelastic}(\omega) \propto \left(\alpha - \sigma_0 \frac{\beta}{Y} \right)^2 \quad (4.10)$$

where Y is Young’s modulus of the fibre, α is the coefficient of linear thermal expansion, σ_0 is the static stress in the fibre due to the suspended load, and $\beta = \frac{1}{Y} \frac{dY}{dT}$ is the thermal elastic coefficient and d is the diameter of the fibre.

For many materials, the value of β is negative, showing a negative correlation between stiffness and temperature, because the particles have more energy to distort inter-particle bonding at higher temperatures. This increases the level of thermoelastic loss experienced if a large positive tensile stress σ_0 is applied to the material. However, fused silica has a β value which is positive (1.52×10^{-4})[36], meaning that the material becomes stiffer as temperature increases. Thermoelastic loss can thus be reduced by application of an appropriate static stress, and in principle nulled entirely when

$$\sigma_0 = \frac{\alpha Y}{\beta} \equiv \frac{W_{load}}{A} \quad (4.11)$$

where W_{load} is weight of the load and A is cross-section of the fibre. For Advanced LIGO, the optimal diameter that cancels thermoelastic noise is $800 \mu\text{m}$.

Instead of maintaining this diameter along the full length of fibre, Advanced LIGO uses silica fibres that vary in diameter to achieve optimal combined noise level. At the ends where the fibre is welded to the test mass, the fibres have a large diameter of 3mm to reduce flexing of the welded joints, where bending energy tends to be concentrated. It then thin to a diameter of 800 μm for 20 mm to minimise thermal noise, while the 596 mm long central section of the fibre is kept to a thinner diameter of 400 μm , as shown in Fig. 10. In the case where some vibration modes of the fibre may be excited by thermal disturbances, the 400 μm diameter design is necessary to keep vibration resonant peaks of the fibre outside the detector's operating band[34].

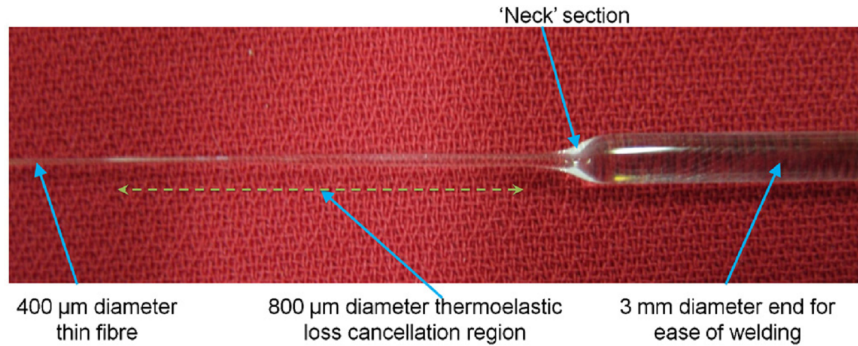


Figure 10: Fused silica fibre with a variable cross section. (Figure adapted from [34])

4.2.2 Reducing coating Brownian noise

Ultra-reflective dielectric coatings for the test masses are required by LIGO in order to minimise optical loss and achieve high levels of laser power amplification (see Section 5.2.2).

The dielectric coatings function based on the interference of light reflected from the different layers of dielectric stack, which consists of a stack of layers with a high refractive index interleaved with layers of a low refractive index, as shown in Fig. 11. In the case of normal incidence, the thicknesses of the layers are chosen to match $\frac{\lambda}{4}$, so that the reflected beams from every interface interfere constructively.

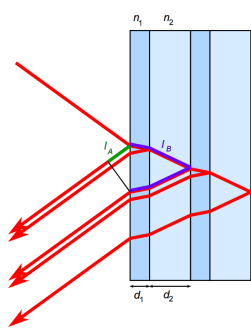


Figure 11: The standard quarter wavelength design. The reflections from the high-index layers have integer multiples of λ in path length difference, and the reflections from the low-index layers have exactly half a wavelength in path length difference. With a 180-degree difference in phase shift at every low-to-high index boundary, they both add up to integer multiples of the wavelength so that the reflections are all in phase, which leads to high reflectivity of the coatings. (Figure adapted from [37])

For good performance (low absorption) at $\lambda_0 = 1064 \text{ nm}$ (the operating wavelength of most gravitational wave detectors), the coatings are made of alternating layers of silica (SiO_2 , $n_{Si} = 1.465$) and tantalum (Ta_2O_5 , $n_{Ta} = 2.035$) doped with 25% titania TiO_2 [38, 39]. Titania-doped tantalum has been shown[40] to have lower mechanical loss, and thus lower thermal noise, than undoped tantalum.

The above quarter-wavelength(QWL) design requires the minimum number of layers to achieve a prescribed reflectivity, but does not yield the lowest thermal noise for a prescribed reflectivity. As Penn et al.[28] showed that the primary source of mechanical dissipation in these coatings was in the tantalum layers rather than in the silica layers or at the interfaces between layers, Eqn. 4.9 shows coating Brownian noise can be reduced if the averaged loss angle of the coating ϕ_c is reduced by having thinner tantalum layers. While this would violate the QWL design, high reflectivity can still be maintained by having an increased number of coatings.

In practice, the thicknesses and number of the coatings are numerically optimized to minimise thermal noise while maintaining high reflectivity. Each time, the layer thickness and number of coatings are adjusted simultaneously; the coating Brownian noise is then calculated analytically using Eqn. 4.9, and the reflectivity is calculated as described in Appendix B.

Fig. 12 shows the result of noise minimisation, with reflectivity kept at $R = 0.999725$. Minimum coating thermal loss is achieved when the ratio of optical path in tantalum and silica is reduced from 1 to 0.45 while increasing number of doublets from 14 to 17. The standard QWL design and optimised design are compared in Fig. 13. This result of optimisation is later confirmed by an experiment conducted by E. Villar et al.[41], which shows that the actual thermal noise with the above optimised coating decreased to $82 \pm 4\%$ of that with the standard QWL design.

Figure 12: Result of optimisation: optimised design (labeled ‘Opt’) v.s. QWL design (labeled ‘QWL’). The ratio of optical path in tantalum and silica is reduced from 1 to 0.45 while increasing number of doublets from 14 to 17 for optimal thermal noise performance. These two parameters must vary simultaneously to maintain a high reflectivity ($R = 0.999725$). (Figure adapted from [39])

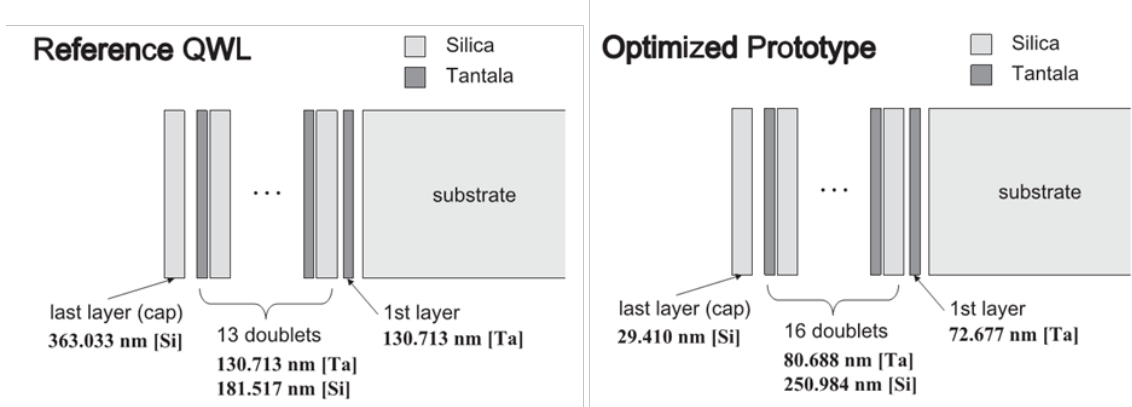
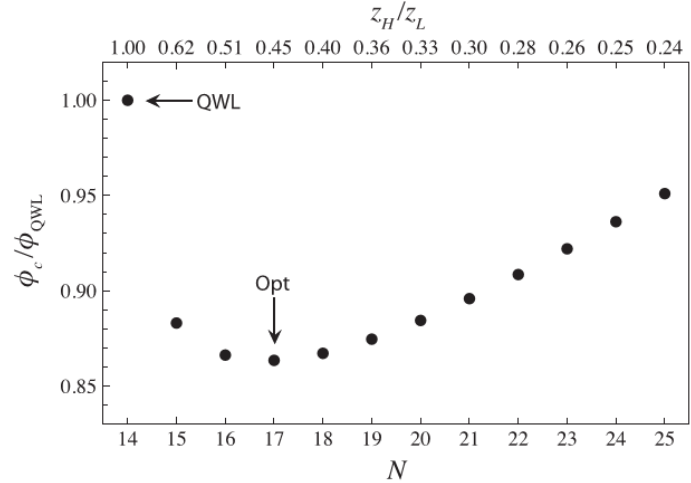


Figure 13: QWL design v.s. optimised design, constructed using the result of optimisation in Fig. 12. The thicknesses of the 1st and last layers are optimised separately from the rest to bring the reflectance to the prescribed level[42]. (Figure adapted from [39])

5 Quantum noise

5.1 Noise Source

Quantum noise refers to the uncertainty that arises from the statistical variations of the laser light in the interferometer. Using Poisson statistics, for any period of observation, T, the expected number of photons produced by the laser is $N \pm \sqrt{N}$ where

$$N = \frac{E_{laser}}{E_{photon}} = \frac{TP\lambda}{hc} \quad (5.1)$$

where P is the laser power and λ is the laser wavelength.

This uncertainty in photon flux gives rise to two noise mechanisms: shot noise and radiation pressure noise.

- **Radiation pressure noise**

When light is reflected off a mirror of mass M the momentum change of the photons causes an impulse on the mirror that results in a force. The statistical fluctuations in the arrival times of the photons thus causes a fluctuating pressure and a fluctuating displacement of the mirror, creating radiation pressure noise.

For a free mirror of mass M and laser power P, the amplitude spectral density of position fluctuations driven by varying radiation pressure obeys[43, 44]

$$S_{RP} \propto \sqrt{\frac{P}{(M\omega^2)^2}} \propto \sqrt{P}. \quad (5.2)$$

where $\omega = 2\pi f$ is the angular frequency at which the measurement is made.

- **Shot noise**

The Michelson interferometer converts differential phase changes in its arms to power change in the interference fringe. A photo detector counts the number of photons in this fringe in a certain measurement time, and produces photo currents proportional to the incident power on it. In this process, the statistical fluctuations of the number of photons results in a photon counting error – the shot noise.

With number of photons, $N \propto P$, and the uncertainty $\sqrt{N} \propto \sqrt{P}$, the amplitude spectrum density of the shot noise obeys

$$S_{shot} \propto \frac{\sqrt{N}}{N} \propto 1/\sqrt{P}. \quad (5.3)$$

While the spectrum of shot noise is independent of frequency, radiation pressure noise falls off as $1/\omega^4$. Consequently, quantum noise is dominated by radiation pressure noise at low frequencies, and at higher frequencies, shot noise is the dominant component of quantum noise and the major limitation on the high frequency performance of gravitational wave detectors[44]. At these frequencies, the priority is to reduce shot noise by increasing the laser power and power recycling, which will be explained in Section 5.2.1. The sum of both noise sources is shown in Fig. 3 as ‘Quantum Noise’.

- **The standard quantum limit**

Equation 5.2 and 5.3 imply that, for a given measurement frequency, there exists a power level P that minimises the combination of the radiation pressure noise and the shot noise. The displacement level that is achieved for this optimisation is called the standard quantum limit (SQL), which gives the theoretical minimum detectable displacement[45]

$$\delta x_{SQL}^2 = \frac{4\hbar\Delta f}{m\omega^2} \quad (5.4)$$

where Δf is the observation bandwidth.

The trade-off between radiation pressure noise and shot noise is a manifestation of uncertainties due to the observer effect in quantum physics³: an initial measurement of the particle's position imparts an unknown momentum to it via radiation pressure, which prevents one from predicting the outcome of a later position measurement. Equation 5.4 translates to a theoretical strain sensitivity of $1.8 \times 10^{-22}/\sqrt{\text{Hz}}$ for the Advanced LIGO[8].

In general, SQL is a fundamental limit on our ability to detect gravitational waves with test masses of a given mass. However, one of the key assumptions to this limit is that there is no position-momentum coupling[46], i.e., no correlation between shot noise and radiation pressure noise. Therefore, measures that introduce coupling between these two types of quantum noise can potentially reduce the noise below SQL. One such example is the addition of a signal recycling mirror, which will be discussed in Section 5.2.2.

5.2 Reducing Quantum Noise

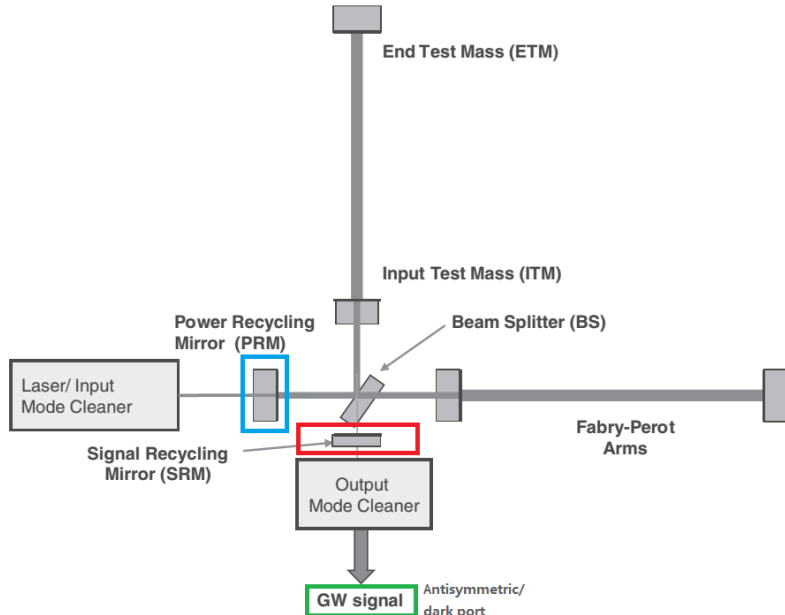


Figure 14: Power recycling mirror (blue), signal recycling mirror (red) and the dark port (green) in the Advanced LIGO interferometer, modified from Fig. 2

5.2.1 Power recycling

At high frequencies where shot noise dominates, increasing the laser power incident in the interferometer can effectively reduce quantum noise (cf. Eqn 5.3). Besides increasing the laser-source power, the equivalent effect can also be achieved by power recycling.

For power amplification to become possible, an interferometric gravitational wave detector is operated under a dark fringe condition, meaning that the reflected beams by the arm mirrors are set to interfere destructively at the detection port (called the ‘antisymmetric’ or ‘dark’ port), highlighted in green in Fig. 14. Consequently, most of the injected laser power is reflected back toward the laser source and ‘recycled’ by inserting a partially reflecting mirror between the laser

³Many authors like Corbitt and Mavalvala[46] and Buonanno and Chen[47] believe it is an equivalent statement of the **Heisenberg uncertainty principle**. There is a slight distinction between the two. The observer effect notes that measurements of certain quantities cannot be made without changing something else in a system. While even Heisenberg himself used such an observer effect as a physical ‘explanation’ of quantum uncertainty, the uncertainty principle has later been found to be a fundamental property of quantum systems, and is not a statement about the observational success of current technology. Therefore, the former offers a better physical description in this case; **mathematically, they yield the same result**.

source and the interferometer, called the power recycling mirror (PRM), highlighted in blue in Fig. 14. Careful choices of reflectivity and position of the recycling mirror lead to significant amplification of laser power in the interferometer.

To quantify power enhancement, we treat an interferometer operating at the dark fringe as a highly reflective compound mirror[9], as shown in Fig. 15. It has complex reflection coefficient $r_{com} \equiv r_2 e^{i\phi_{RT}}$, where $r_2 \equiv |r_{com}|$, and ϕ_{RT} is the phase shift of laser light per round trip within the power-recycling cavity, $\phi_{RT} = (\frac{2\pi}{\lambda}) \times [\text{Total optical path length per round trip}]$. The reflectivity of the compound mirror is $R_{com} = (r_2)^2$.

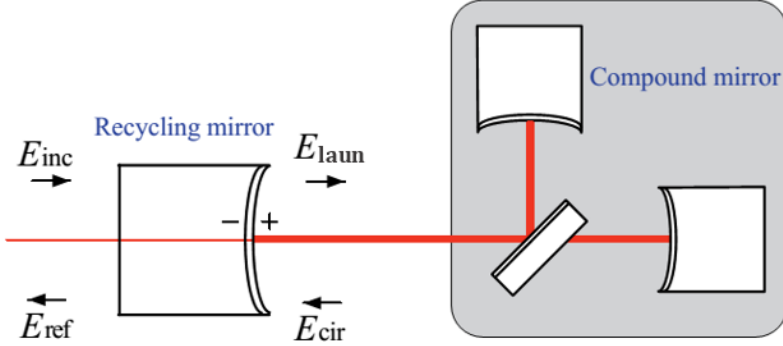


Figure 15: Power recycling cavity; the interferometer is operating at the dark fringe condition and thus can be treated as a highly reflective compound mirror, which forms an EM field resonance cavity with the power recycling mirror. (Figure adapted from [9])

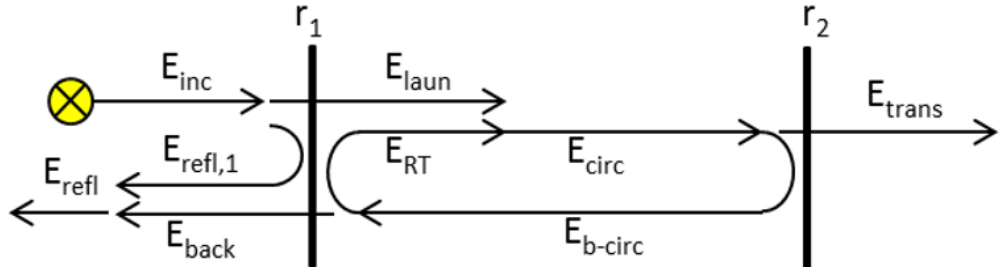


Figure 16: Circulation of EM field in the power recycling cavity (Figure adapted from [48])

This compound mirror effectively forms a Fabry-Perot cavity with PRM, which has reflection coefficient with amplitude r_1 (real, positive), as shown in Fig. 16. Power recycling is achieved by establishing resonance within the cavity, i.e. constructive interference between the light launched into it (with E field E_{laun}) and the light circulating in the cavity (E_{circ}).

At the steady state the fields around the recycling cavity satisfies

$$E_{circ} = E_{laun} + E_{RT} \quad (5.5)$$

with

$$E_{RT} = r_1 r_2 e^{i\phi_{RT}} E_{circ} \quad (5.6)$$

representing the E field after one round trip, and

$$E_{laun} = t_1 E_{inc} \quad (5.7)$$

where t_1 is the transmission coefficient of PRM.

Substituting Eqn. 5.6 and 5.7 into 5.5 gives the amplitude gain of the recycling cavity, g , as

$$g = \frac{E_{circ}}{E_{inc}} = \frac{t_1}{1 - r_1 r_2 e^{i\phi_{RT}}} \quad (5.8)$$

The power recycling gain, G given by

$$G = |g|^2 = \frac{|t_1|^2}{|1 - r_1 r_2 e^{i\phi_{RT}}|^2} \quad (5.9)$$

Maximising G with respect to reflectivity of PRM, $R_1 = r_1^2$, the power recycling gain is the highest when

$$R_1 = R_{com} \quad \text{and} \quad e^{i\phi_{RT}} = 1$$

This gives

$$G_{max} = \frac{1}{1 - R_{com}} \quad (5.10)$$

Eqn. 5.10 shows that the maximum power recycling gain is inversely proportional to the total loss of the compound mirror, $1 - R_{com}$. This drives the need for having high powers reflecting off the test masses and is a reason why very low absorption coatings are needed on the test masses (See Section 4.2.2).

The power recycling scheme of Advanced LIGO, builds up laser power within the cavity by a factor of $G \sim 6000$ [44]. Power recycling, coupled with an increase in the available power of laser, allows up to 800 kW of laser power to circulate in the arm cavities – 20 times higher than in initial LIGO — significantly reducing the high frequency shot noise[8].

5.2.2 Signal recycling

Addition of signal recycling is an upgrade to Advanced LIGO to amplify signal at specific, narrow-banded frequencies, which is valuable for narrowing of the detection bandwidth in detection of continuous wave sources of gravitational radiation[7] and improving sensitivity over a broader range of frequencies.

Sidebands (light with phase shifts) created by gravitational wave signals do not interfere destructively and so appear at the dark port as the output signal. In signal recycling, the signal recycling mirror (SRM) of suitably chosen position and reflectivity is put at the output of the system as shown in Fig. 14. Like PRM, the SRM recycles the sidebands back into the interferometer where they resonate, and hence the signal is amplified over a given bandwidth.

The SRM functions essentially by making phase changes induced on each passing in the interferometer add up coherently. In the case of an incoming gravitational wave signal with angular frequency ω_g , it creates a differential optical path $\delta l \propto \sin(\omega_g t)$ for each round trip of the interferometer, and therefore an oscillating phase shift of the sidebands,

$$\delta\phi(t) = 2\left(\frac{2\pi}{\lambda}\right)\delta l \propto \sin(\omega_g t) \equiv \Re\{e^{-i(\omega_g t - \pi/2)}\}. \quad (5.11)$$

With SRM sending the signal back for N round trips and a total time of τ_s , the phase shift of the signal adds up as

$$\Delta\phi = \sum_{k=0}^N \delta\phi(t = k\tau_s/N). \quad (5.12)$$

In the limit of $\tau_s/N \rightarrow 0$, Eqn. 5.12 becomes

$$\Delta\phi = \int_0^{\tau_s} \delta\phi(t) dt \propto \frac{1}{\omega_g} (1 - \cos(\omega_g \tau_s)). \quad (5.13)$$

Therefore, maximising $|\Delta\phi|$ requires $\tau_s = \pi/\omega_g = \tau_g/2$ [49], where τ_g is the period of the gravitational wave with maximum signal amplification. The phase diagram of maximum resultant phase change is shown in Fig. 17.

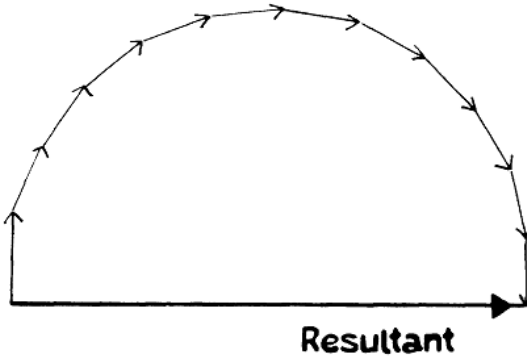


Figure 17: An amplitude-phase diagram for the light emerging from a signal-recycling cavity with $\tau_s = \tau_g/2$. Each vector corresponds to the phase change induced by a continuous gravitational wave on one round trip in the interferometer. The change in angle of each arrow is produced by a change in phase of the gravitational wave. (Figure adapted from [49])

As a result, adjusting the precise position and reflectivity of the SRM allows tuning of frequencies with peak sensitivity by setting the desired storage time τ_s . Such tuning helps broaden the frequency response of the detector and improve its sensitivity at frequencies below 80 Hz and above 200 Hz[1].

As mentioned earlier, addition of SRM enables Advanced LIGO to reach sub-SQL quantum noise levels. Since the early 1970s, many thought that beating the SQL for gravitational wave detectors could only be achieved through radical, non-classical redesigns, like quantum non-demolition speed meter designs[50] or squeezed vacuum injection[51]. However, Buonano and Chen [47, 52, 53] showed that the same effect can be achieved through signal recycling, which allows LIGO to beat the SQL by roughly a factor of two over a limited bandwidth, at the price of increasing noise at other frequencies. Signal recycling introduces dynamic correlation between quantum shot noise and radiation pressure noise, which, according to Buonano and Chen, comes naturally from the ‘nontrivial coupling between the test mass and the signal recycled optical fields’ when resonance is established in the signal recycling cavity. The dynamical properties of the composite optical-mechanical system thus differ from the naive picture of a free test mass subjected to Poissonian radiation pressure. Consequently, direct application of the uncertainty principle on the uncorrelated momentum and position of a free test mass is no longer valid with signal recycling, and the actual quantum noise limit is modestly lower.

6 Further Discussions

We have so far discussed the three most significant noise sources that have been tackled by Advanced LIGO to reach its sensitivity goals. The ultimate result of all these techniques are illustrated in Fig. 18, which shows the calculated LIGO sensitivity curves, from Initial and Enhanced LIGO to Advanced LIGO.

Notably, the lower bound of the detection band is extended from 40 Hz to 10 Hz as a result of seismic noise (Section 3) and thermal noise (Section 4) minimisation. With reduction in quantum noise (Section 5), which limits sensitivity at most of the intermediate frequencies, Advanced LIGO is now 10 times more sensitive than Initial LIGO in the intermediate frequency range. As the detectable volume of the universe scales as the cube of the strain sensitivity, this represents a 1000 times increase in the number of potential astrophysical sources detectable by LIGO.

Advanced LIGO also has a tunable sensitivity shape - a unique feature as a product of signal recycling (Section 5.2.2). Two baseline curves are shown in Fig. 18, one with ‘broadband’ sensitivity and one tuned to have maximum sensitivity in a narrow frequency range at around 1 kHz. This is where the gravitational-wave radiation from many spinning neutron stars and low-mass X-ray binaries is expected to be[54].

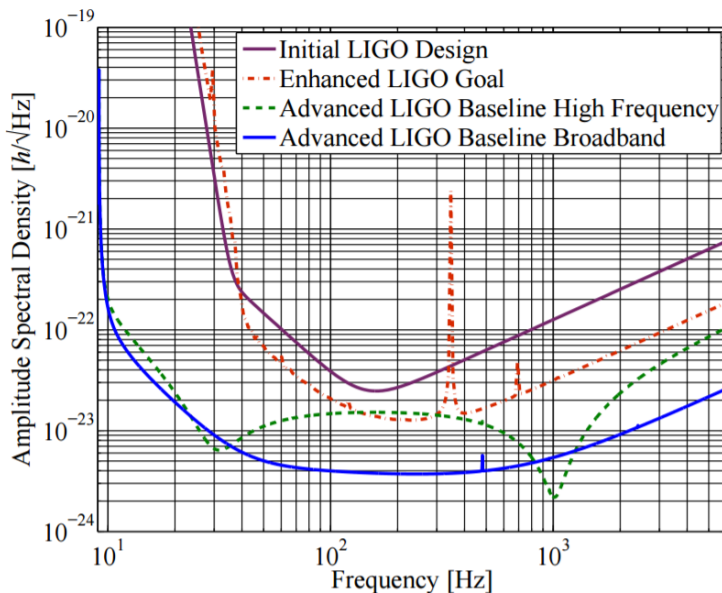


Figure 18: Calculated LIGO sensitivity curves in strain amplitude spectral density. The Enhanced LIGO sensitivity goal is an improvement by roughly a factor of two over initial LIGO above 50 Hz, while Advanced LIGO shows improvement by a factor of 10 and an extension of the lower bound of the detection band. The tunable Advanced LIGO sensitivity is shown as the untuned ‘Baseline Broadband’ and the fine-tuned ‘Baseline High Frequency’. (Figure adapted from [54])

Besides seismic, thermal and quantum noises, there are also other types of noise present at Advanced LIGO that have not been addressed in this paper, although their impact is often more than an order of magnitude smaller than that of the dominant ones. Such examples include gas noise from residual gases in vacuum chambers, charging noise from electrostatic actuation on the test masses, Laser amplitude and frequency noise, beam jitter (random transverse motions of the Laser beam), etc., all being carefully modeled and controlled[1] at Advanced LIGO. Additionally, some noise sources remain unidentified: at frequencies below 100 Hz, there is currently a significant gap between the measured strain noise and the root-square sum of investigated noises[1]. Future work is required to find these remaining noise sources.

7 Concluding Remarks

The review has presented some of the most important experimental techniques adopted at LIGO for high-sensitivity measurements in gravitational wave detection, targeting seismic, thermal and quantum noise minimisation. Currently, the overall performance of Advanced LIGO is dominated at most frequencies by quantum noise, with a contribution at mid-frequencies from the internal thermal noise of the coatings of the test masses.

The current design, with modest enhancements, is believed to have pushed the LIGO interferometer architecture to its technical endpoint.[55] it has reached the sensitivity limit of an interferometer based on familiar technology - a Fabry-Perot Michelson configuration with external optical readout using room temperature transmissive optics.

In the future, further advances are expected to come from some of the unfamiliar and more radical designs, such as cryogenic optics and suspensions, purely reflective optics, and non-classical quantum noise minimising designs like quantum non-demolition speed meters. These later developments will be timely for instruments to be developed in the second decade of this century.

References

- [1] D.V.Martynov, et al., 2016, *The Sensitivity of the Advanced LIGO Detectors at the Beginning of Gravitaional Wave Astronomy*, Phys. Rev. D93, 112004
- [2] B. P. Abbott, et al., 2016, LIGO Scientific Collaboration and Virgo Collaboration, *Observation of Gravitational Waves from a Binary Black Hole Mergers*, Phys. Rev. Lett. 116, 061102
- [3] M. E. Gertsenshtain and V. I. Pustovoit, 1962, Sov. Phys. -JETP 16, 433
- [4] F Acerne, M Alshourbagy, et al., 2008, *Virgo status*. Class. Quantum Grav, 25:4001
- [5] B Willke, 2002, *The GEO 600 Gravitational Wave Detector*. Class. Quantum Grav, 19:11
- [6] LIGO Scientific Collaboration, 2014, LIGO Document P1400177,
- [7] Jim Hough and Sheila Rowan, 2005, *Laser interferometry for the detection of gravitational waves*, J. Opt. A: Pure Appl. Opt. 7, S257-S264
- [8] S. J. Waldman, for the LIGO Scientific Collaboration, 2011, *The Advanced LIGO Gravitational Wave Detector*, LIGO Document P0900115
- [9] Masaki Ando, 1998, *Power Recycling for an Interferometric Gravitational Wave Detector*, PhD Thesis, University of Tokyo
- [10] Calum Torrie, 2000, *Development of Suspensions for the GEO 600 Gravitational Wave Detector*, PhD Thesis, University of Glasgow
- [11] S. Braccini et al., 1993, Rev. Sci. Instrum. 64, 310; M. Beccaria et al., 1997, Nucl. Instrum. Methods Phys. Res. A 394, 397.
- [12] F. Matichard, et al., 2015, *Seismic isolation of Advanced LIGO: Review of strategy, instrumentation and performance*, Class. Quantum Grav. 32 185003
- [13] Gregory M Harry and the LIGO Scientific Collaboration, 2010, *Advanced LIGO: the next generation of gravitational wave detectors*, Class. Quantum Grav. 27 084006
- [14] Wensheng Hua, et al., 2004, *Polyphase FIR Complementary Filters for Control Systems*, Proceedings of ASPE Spring Topical Meeting on Control of Precision Systems, pp. 109-114
- [15] Ryan DeRosa, et al., 2012, *Global Feed-Forward Vibration Isolation in a km scale Interferometer*, Class. Quantum Grav. 29 215008
- [16] Hazel J, Kawamura S and Raab F, 1996, *Suspension Preliminary Design*, LIGO Document T960074
- [17] M. V. Plissi, et al., 2000, *GEO 600 triple pendulum suspension system: Seismic isolation and control*, Review of Scientific Instruments 71, 2539
- [18] Norikatsu Mio, 1992, *Mechanical Transfer Function of a Pendulum Suspended with a Finite-Mass Wire*, Jpn. J. Appl. Phys. 31 1243
- [19] Andrew Thomas, 2004, *Characterization of an Advanced LIGO Quadruple Pendulum System*, Thesis, Massachusetts Institute of Technology, <http://hdl.handle.net/1721.1/28329>
- [20] N A Robertson, et al., 2002, *Quadruple suspension design for Advanced LIGO*, Class. Quantum Grav. 19, 4043–4058
- [21] Peter R. Saulson, 1990, *Thermal noise in mechanical experiments*, Phys. Rev. D 42, 2437
- [22] Herbert Callen and Theodore A. Welton, 1951, *Irreversibility and Generalized Noise*, Phys. Rev. 83, 34

- [23] A. S. Nowick and B. S. Berry, *Anelastic Relaxation in Crystalline Solids* (Academic, New York, 1972)
- [24] Yu. Levin, 1998, *Internal thermal noise in the LIGO test masses: A direct approach*, Phys. Rev. D 57 659
- [25] Gregory M Harry, et al., 2002, *Thermal noise in interferometric gravitational wave detectors due to dielectric optical coatings*, Class. Quantum Grav. 19 897
- [26] Maria Principe, 2014, *Minimum Noise Optical Coatings for Interferometric Detectors of Gravitational Waves*, Proceedings of the 2014 IEEE International Workshop on Metrology for Aerospace
- [27] Ting Hong, et al., 2013, *Brownian Thermal Noise in Multilayer Coated Mirrors*, Phys. Rev. D 87, 082001
- [28] Steven D Penn, et al., 2003, *Mechanical loss in tantalum/silica dielectric mirror coatings*, Class. Quantum Grav. 20 2917
- [29] Riccardo DeSalvo, 2002, *Path-finding towards a cryogenic interferometer for LIGO*, Class. Quantum Grav. 19 2021
- [30] Kentaro Somiya, 2012, Class. Quantum Grav. 29 124007
- [31] Braginsky V B, et al., 1996, *Energy dissipation in the pendulum mode of the testmass suspension of a gravitational wave antenna*, Phys. Lett. A 218 164–6
- [32] Owan S, et al., 1997, *The quality factor of natural fused quartz ribbons over a frequency range from 6 to 160 Hz*, Phys. Lett. A 227 153–8
- [33] Merrill L, 2008, *A study of thermal noise for enhanced LIGO*, LIGO Document P080083
- [34] A Cumming, et al., 2012, *Design and development of the advanced LIGO monolithic fused silica suspension*, Class. Quantum Grav. 29 035003 (18pp)
- [35] Cagnoli G and Willems P, 2002, *Effects of nonlinear thermoelastic damping in highly stressed fibres*, Phys. Rev. B 65 174111
- [36] A Cumming, et al., 2009, *Finite element modelling of the mechanical loss of silica suspension fibres for advanced gravitational wave detectors*, Class. Quantum Grav. 26 215012
- [37] Wikipedia, 4 Aug. 2008, *Dielectric mirror*, retrieved from https://en.wikipedia.org/wiki/Dielectric_mirror
- [38] Gregory M Harry (for the LIGO Scientific Collaboration), 2010, *Advanced LIGO: the next generation of gravitational wave detectors*, Class. Quantum Grav. 27 084006
- [39] Akira E. Villar, et al., 2010, *Measurement of thermal noise in multilayer coatings with optimized layer thickness*, Phys. Rev. D 81, 122001
- [40] Gregory M Harry, et al., 2007, *Titania-doped tantalum/silica coatings for gravitational-wave detection*, Class. Quantum Grav. 24 405
- [41] A.E. Villar et al., 2010, *Measurement of Thermal Noise in Multilayer Coatings with Optimized Layer Thickness*, Phys. Rev. D 81, 122001
- [42] V. Pierro et al., 2009, *Coating Optimization Status*, LIGO Document G0900205
- [43] Carlton M. Caves, 1980, *Quantum-mechanical noise in an interferometer*, Phys. Rev. D 23, 1693
- [44] David J. Ottaway and Steven D. Penn, *Gravitational wave detection*, 2012, Optical Coatings and Thermal Noise in Precision Measurement, Cambridge University Press

- [45] W A Edelstein, et al., 1978, *Limits to the measurement of displacement in an interferometric gravitational radiation detector*, J. Phys. E: Sci. Instrum. 11 710
- [46] Thomas Corbitt and Nergis Mavalvala, 2004, *Quantum noise in gravitational-wave interferometers*, J. Opt. B: Quantum Semiclass. Opt. 6, S675–S683
- [47] Alessandra Buonanno and Yanbei Chen, 2001, *Quantum noise in second generation, signal-recycled laser interferometric gravitational-wave detectors*, Phys. Rev. D 64, 042006
- [48] Ismail, N., Kores, C. C., Geskus, D., Pollnau, M., 2006, *Fabry-Pérot resonator: spectral line shapes, generic and related Airy distributions, linewidths, finesse, and performance at low or frequency-dependent reflectivity*, Optics Express. 24 (15): 16366–16389
- [49] Brian J. Meers, 1988, *Recycling in laser-interferometric gravitational-wave detectors*, Phys. Rev. D 38, 2317
- [50] V. B. Braginsky, M. L. Gorodetsky, F. Ya. Khalili, and K. S. Thorne, 2000, *Dual-resonator speed meter for a free test mass*, Phys. Rev. D 61, 044002
- [51] C. M. Caves, 1981, Phys. Rev. D 23, 1693; W. G. Unruh, 1982, in *Quantum Optics, Experimental Gravitation, and Measurement Theory*, edited by P. Meystre and M. O. Scully (Plenum, New York), p. 647; M. T. Jaekel and S. Reynaud, 1990, Europhys. Lett. 13, 301.
- [52] Alessandra Buonanno and Yanbei Chen, 2001, *Optical noise correlations and beating the standard quantum limit in advanced gravitational-wave detectors*, Class. Quant. Grav. 18, L95-L101
- [53] Alessandra Buonanno and Yanbei Chen, 2002, *Signal recycled laser-interferometer gravitational-wave detectors as optical springs*, Phys. Rev. D 65 042001
- [54] J R Smith for the LIGO Scientific Collaboration, 2009, *The Path to the Enhanced and Advanced LIGO Gravitational-Wave Detectors*, Class. Quantum Grav. 26 114013
- [55] Advanced LIGO website, 24 Oct. 2016, *An Overview of Detector Upgrades*, retrieved from <https://www.advancedligo.mit.edu/overview.html>
- [56] Peter R. Saulson, 1984, *Terrestrial gravitational noise on a gravitational wave antenna*, Phys. Rev. D 30, 732
- [57] Scott A. Hughes and Kip S. Thorne, 1998, *Seismic gravity-gradient noise in interferometric gravitational-wave detectors*, Phys. Rev. D 58, 122002
- [58] Jennifer C. Driggers, Jan Harms, and Rana X. Adhikari, 2012, *Subtraction of Newtonian noise using optimized sensor arrays*, Phys. Rev. D 86, 102001
- [59] Fidecaro F, 2001, LIGO Document G010317-00
- [60] S. J. Orfanidis, 1 Aug. 2016, *Electromagnetic waves and antennas*, retrieved from <http://www.ece.rutgers.edu/~orfanidi/ewa/>

Appendix A More on Gravitational Gradient Noise

Seismic motion in the earth leads to fluctuations in local gravitational fields around the test masses, which give rise to varying gravitational forces experienced by the test masses, which is called the gravitational gradient noise.

In 1984, Saulson[56] used laws of Newtonian gravity to show that, in the frequency domain, a displacement $\Delta\tilde{X}(\omega)$ of a point in the Earth from its equilibrium position leads to fluctuations $\Delta\tilde{g}(\omega)$ in the gravitational field along the direction of arm length, given by

$$|\Delta\tilde{g}(\omega)| = 4\pi G \rho_e \beta |\Delta\tilde{X}(\omega)| \quad (\text{A1})$$

where ω , G , ρ_e are angular frequency, gravitational constant and density of earth respectively. Saulson estimated β as a constant geometric factor of $1/\sqrt{3}$, and Hughes and Throne[57] later improved the estimation by introducing a varying $\beta(\omega)$ with values 0.35-0.6 at quiet times and 0.15-1.4 at noisy times at LIGO sites. Such adjustments account for a slight reduction of the noise due to the height of the test masses above the Earth's surface and weak interactions between the test masses.

The fluctuating gravitational force drives the differential arm-length motion, $\Delta\tilde{x}(\omega)$ according to

$$|\Delta\tilde{x}(\omega)| = \frac{|\Delta\tilde{g}(\omega)|}{\sqrt{(\omega^2 - \omega_0^2)^2 + \omega^2/\tau^2}} \quad (\text{A2})$$

where ω_0 is the resonant angular frequency and τ is the damping time. At frequencies $\omega > \omega_0$, $\tilde{x}(f)$ gives the gravitational gradient displacement noise spectrum:

$$|\Delta\tilde{x}(f)| \approx \frac{|\Delta\tilde{g}(f)|}{(2\pi f)^2} \quad \text{where } f = 2\pi\omega \geq 3 \text{ Hz} \quad (\text{A3})$$

At $f=10$ Hz, using Eqn. 3.1, A1 and A3 and $\rho_e \approx 1800 \text{ kg m}^{-3}$, we obtain a gravitational gradient noise level at the order of $\sim 10^{-19} \text{ m}/\sqrt{\text{Hz}}$.

There is no known way to shield the detector's test masses from gravitational gradient noise[58]. While schemes to monitor such gradients and cancel out their effects on the interferometers have been proposed[59], these are far away from implementation. Such noise remains as one of the limiting noise sources of the Advanced LIGO in the frequency range 10-20 Hz[1].

Appendix B Reflectivity of Multilayer Dielectric Coatings: an Analytic Solution

Based on plane-wave solutions to the Maxwell's Equations in dielectric materials, for time-harmonic ($e^{i\omega t}$) normal plane wave incidence, the electric and magnetic fields at the i th interface of a coating are related to the fields at the $(i+1)$ th one by the propagation matrix of the i th layer, \mathbf{M}_i [60]:

$$\begin{pmatrix} E_i \\ H_i \end{pmatrix} = \begin{pmatrix} \cos(\delta_i) & in_i^{-1}Z_0\sin(\delta_i) \\ in_i^{-1}Z_0\sin(\delta_i) & \cos(\delta_i) \end{pmatrix} \begin{pmatrix} E_{i+1} \\ H_{i+1} \end{pmatrix} \quad (\text{B1})$$

where $Z_0 = \sqrt{\mu_0/\epsilon_0}$ is the characteristic impedance of the vacuum, n_i is the refractive index of the layer, and $\delta_i = 2\pi(d_i/\lambda_i)$ is the optical path length ('phase thickness') where d_i is thickness of the i th layer and $\lambda_i = \lambda_0/n_i$. Fig. 19 below is an illustration of wave propagation in a multilayer coating.

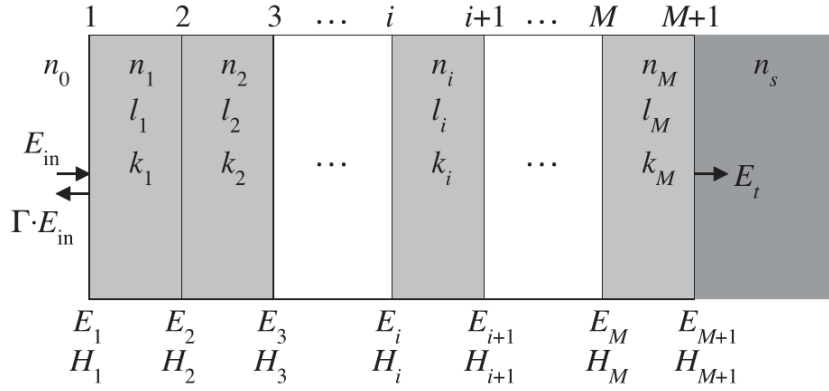


Figure 19: Electromagnetic waves propagating in M -layer dielectric coatings. l is the layer thickness, n is the refractive index, and k is the wave vector.

The effective input impedance of the coating, $Z_i n = E_1/H_1$, can then be obtained from chain multiplication of the propagation matrices of all the layers:

$$\begin{pmatrix} E_1 \\ H_1 \end{pmatrix} = \mathbf{M}_1 \cdot \mathbf{M}_2 \cdots \mathbf{M}_M \begin{pmatrix} E_{M+1} \\ H_{M+1} \end{pmatrix}, \quad \text{where } \begin{pmatrix} E_{M+1} \\ H_{M+1} \end{pmatrix} = \begin{pmatrix} E_t \\ (n_s/Z_0)E_t \end{pmatrix} \quad (\text{B2})$$

The reflectivity of the coating in terms of the input impedance is given by

$$R = \left| \frac{Z_{in} - Z_0}{Z_{in} + Z_0} \right|^2. \quad (\text{B3})$$